INCLUSIVE PUBLISHING TRUSTED SCIENCE
PURPOSE-LED PUBLISHING™

PAPER • **OPEN ACCESS**

Effect of FABr over-stoichiometry on the morphology and optoelectronic properties of wide-bandgap $FAPbBr_3$ films

To cite this article: G Ammirati *et al* 2026 *Nano Ex.* **7** 025013

View the article online for updates and enhancements.

You may also like

- Tailoring the orientation of perovskite crystals via adding two-dimensional polymorphs for perovskite solar cells
Renjun Guo, Ali Buyruk, Xinyu Jiang et al.
- *(Invited)* Breaking Centro-Symmetry in Formamidinium Lead Triiodide ($FAPbI_3$) Films with Preferred Oriented Grains
Hyunjung Shin
- Enhanced Efficiency and Stability of Inverted Solar Cells Utilizing Pure -FAPbI3 Single Crystal Perovskite
Jin Hyuck Heo, Jin Kyoung Park, Woo-Sik Kim et al.

kiutra

Millikelvin characterization for superconducting devices

L-TYPE RAPID

- **< 4 hrs** sample loading and cooldown to base
- **50 mK** base temperature
- **30 min** warm up and sample exchange

Find out more →



This content was downloaded from IP address 160.80.176.104 on 29/09/2026 at 14:41

NANO EXPRESS

Check for updates

OPEN ACCESS

RECEIVED
10 February 2026

REVISED
14 May 2026

ACCEPTED FOR PUBLICATION
18 May 2026

PUBLISHED
28 May 2026

Original content from this work may be used under the terms of the Creative Commons Attribution 4.0 licence.

Any further distribution of this work must maintain attribution to the author(s) and the title of the work, journal citation and DOI.

PAPER

Effect of FABr over-stoichiometry on the morphology and optoelectronic properties of wide-bandgap $FAPbBr_3$ films

G Ammirati[1], F Martelli[1], F Toschi[1], S Turchini[1], P O'Keeffe[2], A Paladini[2], F Matteocci[3], J Barichello[1], D Di Girolamo[3], S Piccirillo[4], A Di Carlo[1,3] and D Catone[1,*]

[1] Istituto di Struttura della Materia—CNR (ISM-CNR), EuroFEL Support Laboratory (EFSL), Via del Fosso del Cavaliere 100, Rome 00133, Italy
[2] Istituto di Struttura della Materia—CNR (ISM-CNR), EuroFEL Support Laboratory (EFSL), Monterotondo Scalo 00015, Italy
[3] Department of Electronic Engineering, Centre for Hybrid and Organic Solar Energy (CHOSE), Tor Vergata University of Rome, Via del Politecnico 1, Rome 00133, Italy
[4] Department of Chemical Sciences and Technologies, Tor Vergata University of Rome, Via della Ricerca Scientifica, Rome 00133, Italy
* Author to whom any correspondence should be addressed.

E-mail: daniele.catone@cnr.it

Keywords: Perovskite thin films, defect passivation, semitransparent solar cells

Supplementary material for this article is available online

Abstract

In this study, we investigate the impact of formamidinium bromide (FABr) over-stoichiometry in the precursor solution on the optoelectronic properties and morphology of the resulting films of formamidinium lead bromide. Optical characterization, including steady-state absorption, photoluminescence (PL), and femtosecond transient absorption spectroscopy, reveals a systematic blueshift in emission energy with increasing FABr content, attributed to compositional variations induced by FABr excess. The excess of FABr also induces the reduction of defects associated with radiative recombination. Indeed, the stoichiometric film exhibits a PL band due to donor–acceptor pair (DAP) recombination as identified by the typical blueshift for increasing excitation intensity, whereas FABr-enriched samples show no evidence of DAP emission. Additionally, morphological characterization shows a reduction in grain size with increasing FABr excess, indicating a trade-off between improved electronic quality and enhanced structural disorder. The film synthesized with a 5% excess of FABr provides the optimal balance, yielding the highest power conversion efficiency (6.26%), average visible transmittance (61.6%), and light utilization efficiency (3.85%). These results demonstrate that fine-tuning the precursor stoichiometry represents a simple yet effective strategy to enhance the optoelectronic quality and performance of semitransparent perovskite solar cells.

1. Introduction

Hybrid metal halide perovskites (MHPs) have revolutionized photovoltaic technology over the last decade, because of their exceptional optoelectronic properties. Indeed, MHPs show high absorption coefficients in the visible range ($\sim 10^5$ cm^{-1}), band gap tunability, long carrier diffusion length (>1 μm), long carrier lifetime (~ 1 μs), and unusually high defect tolerance [1–6]. These properties counterbalance the moderate carrier mobility (~10 cm^2 V^{-1} s^{-1}), which is lower with respect to traditional semiconductors (e.g. 1000 cm^2 V^{-1} s^{-1} for Si) [7]. MHPs are usually employed in photovoltaic applications as thin films of a few hundred nanometers in the form of a polycrystalline structure composed of micrometer-sized grains. These features collectively make halide perovskites highly attractive for a variety of optoelectronic applications, including photovoltaics, LEDs and photodetectors. Furthermore, the films

© 2026 The Author(s). Published by IOP Publishing Ltd

are obtained by means of low-cost fabrication methods such as spin coating, blade coating, screen printing, or inkjet printing [8–11]. Consequently, extensive research effort has been dedicated to optimizing their compositional engineering, morphology control, and device integration.

Among the family of perovskite absorbers, wide-bandgap compositions such as formamidinium lead bromide ($FAPbBr_3$) have gained particular interest for applications in semitransparent solar cells. Moreover, the large bandgap (∼2.3 eV) of $FAPbBr_3$ is particularly well suited to harvesting the high-energy portion of the solar spectrum, making this material an ideal candidate for a top-cell absorber in tandem photovoltaic devices [12, 13]. Nonetheless, a significant challenge in photovoltaic applications of wide-bandgap perovskites is the limited increase in open-circuit voltage compared to their optical bandgap [14]. This voltage deficit primarily originates from unfavorable alignment of energy levels between the absorber and the adjacent charge transport layers, as well as significant non-radiative recombination within the active material [15]. In particular, non-radiative recombination is associated with grain boundaries, halide vacancies, interstitial defects, and other point defects [16, 17].

To mitigate those losses, different strategies have been explored, ranging from advanced interface engineering to the use of multifunctional additives [18–23]. For instance, recent studies have demonstrated that incorporating graphene-doped TiO_2 as an electron transport layer or using imidazole-based additives can significantly enhance charge extraction, passivate defects at grain boundaries, and improve device stability [24]. Furthermore, the introduction of specialized buffer layers, such as cubic silicon carbide, has been proposed to optimize energy level alignment and to reduce interfacial recombination in lead-free and bromine-rich systems [25]. While these treatments are highly effective, precursor engineering through stoichiometric control remains a fundamental yet versatile route to directly tune the crystallization kinetics and the defectivity of the material.

Within this framework, precursor engineering via controlled over-stoichiometry has emerged as an effective strategy to improve the optoelectronic quality of metal–halide perovskites. For instance, $MAPbI_3$ films fabricated with an excess of methylammonium iodide show the formation of defect-passivating surface layers, which lead to suppression of non-radiative recombination and enhancement of the charge carriers' mobility [26]. Similarly, the introduction of excess formamidinium bromide in $FAPbBr_3$ nanocrystals refill bromine and formamidinium vacancies, resulting in a substantial increase in photoluminescence quantum yield and more balanced charge transport due to a reduced density of insulating organic ligands [27]. Despite these promising results, the role of precursor over-stoichiometry in governing the polycrystalline morphology, defect landscape, and electronic properties of $FAPbBr_3$ thin films specifically tailored for photovoltaic applications remains insufficiently explored.

In this paper, we investigate how different levels of FABr excess (+5% and +10%) in the synthesis of the active material affect the crystallization and the optical properties of the $FAPbBr_3$ thin films. By combining morphological characterization, steady-state and temperature-dependent photoluminescence (PL), optical absorption, and transient absorption, we provide deeper insights into the role of the formamidine bromide (FABr) stoichiometry employed in semitransparent photovoltaic applications.

2. Experimental methods

2.1. Sample preparation, synthesis of the materials and device fabrication

$FAPbBr_3$ thin films were deposited onto ITO conductive substrates (Kintec company, 1.1 mm thick, 10 Ω/sq^{-1} of sheet resistance). The substrates were first cut into squares of 2.5 × 2.5 cm and then washed using a sequential cleaning procedure, first in a soap (5% in volume) and water solution, then in deionized water, and finally in isopropanol using ultrasonic baths of 10 min to remove organic compounds and dust. Before depositing the perovskite, the cleaned substrates were soaked under a UV-light treatment for 30 min to improve the surface wettability to obtain a good perovskite film deposition. 1.3 M FABr (Dyesol) and 1.3 M $PbBr_2$ (TCI) were dissolved in a vial of DMSO and left stirring all night. $FAPbBr_3$ deposition was performed under N_2 atmosphere. The substrates were first heated to 60 °C, and then, 80 μl of the perovskite solution was dropped on the surface and spin-coated at 4000 rpm for 20 s. The solvent quenching method was employed to enhance the perovskite crystallization, and 200 μl of ethyl acetate was dropped 10 s after the initiation of the spin. The substrates were then annealed at 80 °C for 10 min. This procedure was followed to fabricate the stoichiometric sample of $FAPbBr_3$ (Control), while for the samples synthesized with an excess of FABr%, concentrations of 1.365 M FABr (a 5% excess) and 1.43 M FABr (a 10% excess) were used for the growth of the FABr 5% and FABr 10% samples, respectively.

The solar cells were fabricated using perovskite films prepared as previously described. The remaining layers of the photovoltaic devices—namely, the electron transport layer, the hole transport layer, and

the top electrode—were deposited following the procedures reported in [28]. As the aim of this study is to isolate the effect of FABr over-stoichiometry on the perovskite absorber rather than maximize photovoltaic performance through device engineering, we did not perform a dedicated optimization of the device stack. The device performance should therefore be interpreted in a comparative framework within a fixed architecture, which was not specifically re-engineered for this work.

2.2. Steady-state optical spectroscopy

The absorbance spectra of thin films were acquired with a Shimadzu UV-VIS spectrometer (model UV-2700) in combination with the Shimadzu multipurpose large-sample compartment (MPC-2600 A) in the 220–850 nm range. These units were used for transmittance and diffuse and specular reflectance measurements.

The average visible transmittance (AVT) of the semitransparent devices was determined following the procedure outlined in ISO 9050:2003. See details in section S.1 of Supporting Information (SI).

2.3. Scanning electron microscopy (SEM) and x-ray diffraction (XRD)

A Field emission scanning electron microscope (FESEM—ZEISS SIGMA 300) was used for the morphological characterization of the samples, using an acceleration voltage of 10 kV and a working distance of 13 mm. The samples were mounted on aluminum stubs using conductive carbon tape and the images were all acquired with the same magnification (25kX), to compare their grain-size distributions, which were analyzed using Gwyddion software [29].

XRD patterns were acquired using a Rigaku SmartLabSE diffractometer equipped with a Cu Kα radiation source, in the 2θ range of 5°–60°.

2.4. Photoluminescence

PL was performed at 12 K in a closed-cycle He cryostat. A PID controller was used to regulate the temperature between 12 K and RT for temperature-dependent measurements. The samples were excited using a continuous-wave laser at 405 nm (Matchbox 2 series). The laser beam was focused on the sample with a spot size of 100 μm, and the PL was collected by a telescope into a monochromator (HORIBA Jobin Yvon—iHR320) with a focal length of 320 mm, and a spectral range of 350 nm–1100 nm with a 1200 gr mm^{-1} grating. Suitable filters were used to eliminate the laser light scattered by the sample.

2.5. Femtosecond transient absorption spectroscopy (FTAS)

FTAS was carried out using an amplified femtosecond laser source delivering 35 fs pulses at a 1 kHz repetition rate with an average power of 4 W, centered at 800 nm. Tunable pump pulses were produced via an optical parametric amplifier. A white-light supercontinuum probe covering the 360–780 nm range was obtained by focusing approximately 3 μJ of the 800 nm beam into a rotating CaF_2 crystal. Both the pump and probe beams were focused onto the sample, with spot diameters of about 200 μm and 150 μm, respectively. The time delay between pump and probe pulses was adjusted by varying the probe optical path length, yielding an overall instrument response of roughly 50 fs. Further experimental details are available elsewhere [30, 31].

3. Results and discussion

Figure 1(a) depicts the absorbance of the different samples (Control, FABr +5%, and FABr +10%), which shows a blueshift of the optical onset from 2.273 eV to 2.280 eV, and then to 2.296 eV with the increase of the FABr excess. The onset of the signal was set at the intercept (orange, green, and blue stars, respectively, for Control, FABr +5%, and FABr +10%) between the absorption peak and the low-energy tail related to the background scattering. The steady-state absorption spectrum of the Control sample exhibits a distinct excitonic feature, which becomes less pronounced as the FABr excess increases. Figure 1(b) reports the corresponding absorption coefficient. The absorption coefficient for each film was estimated according to equation (1):

$$\alpha(\hbar\omega) = \frac{-\mathrm{In}\left(\frac{T(\%)}{100-R(\%)}\right)}{t} \quad (1)$$

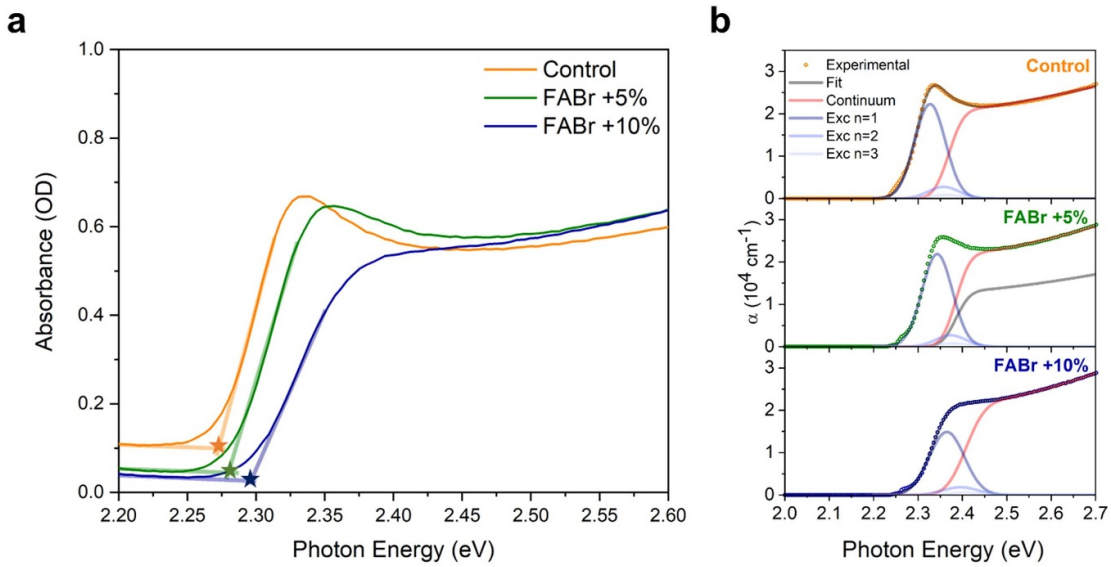


Figure 1. (a) Steady-state absorbance spectra of the control, FABr +5% and FABr +10% samples (see text for details); (b) absorption coefficient of the control, FABr +5%, and FABr +10% films (orange, green and blue scatter, respectively). The data were fitted using the Elliott model (black line), which is further decomposed into contributions from the continuum states (red line) and the three excitonic states (blue line). See text for the details.

Table 1. Absorption curves fitting parameters evaluated with the Elliott model as electronic bandgap (E_g=), exciton binding energy (E_b), Gaussian broadening of the excitonic (σ_x) and continuum (σ_c) contributions, and the coefficient b.

Material	E_g (eV)	E_b (meV)	σ_X (meV)	σ_c (meV)	b(eV^{-1})
Control	2.368	40 ± 5	34	26	0.69
FABr +5%	2.385	40 ± 5	33	25	0.79
FABr +10%	2.406	40 ± 5	39	33	0.91

where T is the transmittivity, R the reflectivity, and t the thickness of the films measured using a Bruker Dektat XT profilometer, yielding an average value of 250 nm for all samples (see figure S6). The sub-bandgap intensity was set to zero to remove the scattering contribution to the spectra. Each steady-state absorption spectrum was decomposed into two components: an excitonic transition and a continuum electronic transition, both convolved with Gaussian broadening functions. Details of the fitting procedure following an Elliot-based excitonic absorption model are reported in section S.2 of SI and in our previous works [32, 33].

From this analysis, several key optical parameters were extracted: the bandgap (E_g), the Gaussian broadening of excitonic (σ_x) and continuum (σ_c) contributions, as well as the coefficient b that takes into account the non-parabolicity of the bands. In the fitting procedure, the exciton binding energy was kept fixed within 40 ± 5 meV, as variations within this range produced essentially identical results. All other parameters were left free to vary. The resulting values are summarized in table 1.

The analysis of the absorption spectra reveals a clear evolution of the optical properties with increasing FABr incorporation. The bandgap increased from 2.368 eV in the Control sample to 2.406 eV in the FABr +10% film, indicating a blueshift of about 40 meV. This shift suggests that FABr incorporation modified the electronic structure, likely through compositional or structural changes within the perovskite lattice. Since the fitting procedure yielded comparable results within the range of 40 ± 5 meV and the exciton binding energy can be considered approximately constant in all samples, we assume that the dielectric screening and effective masses are not strongly affected by the excess of FABr. More pronounced changes were instead observed in the broadening parameters: while the Control and FABr +5% films exhibit similar excitonic and continuum broadening, both contributions significantly increased in the FABr +10% sample. The increase of the coefficient b from 0.69 to 0.91 eV^{-1} is consistent with the changes of the electronic structure induced by the FABr excess. The slight difference between the blueshift extracted from the absorption onset and that obtained from Elliott fitting (23 meV and 38 meV, respectively) can be explained by the different approaches used: while the onset is sensitive to

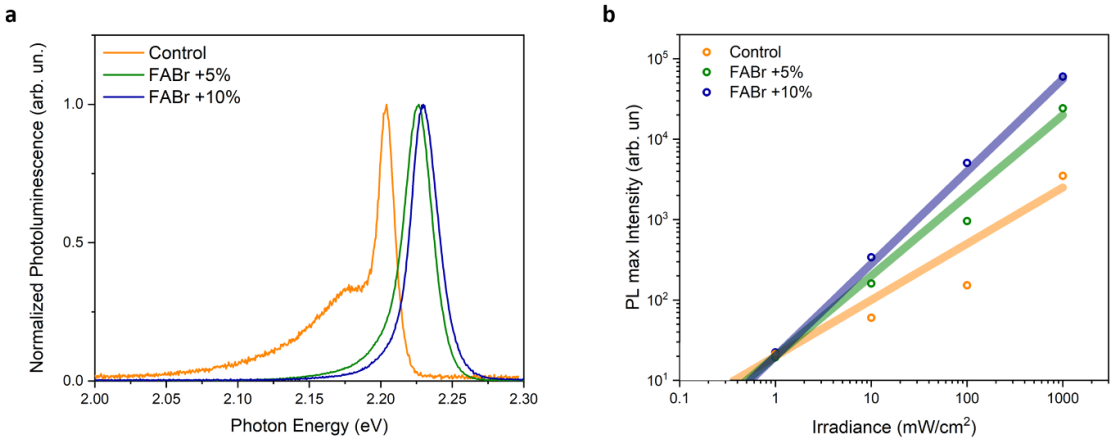


Figure 2. (a) PL spectra, normalized at the maximum intensity, acquired at 12 K for the Control, FABr +5% and FABr +10% thin films and with an excitation laser at 405 nm at an irradiance of 100 mW cm^{-2}; (b) PL main peak intensity as a function of the excitation laser irradiance for all samples.

Table 2. Power-law exponent (n) obtained by fitting the PL intensity of the main emission peak as a function of the excitation irradiance for Control, FABr +5%, and FABr +10%.

	Control	FABr +5%	FABr +10%
n	0.70 ± 0.18	1.00 ± 0.09	1.14 ± 0.02

spectral broadening and disorder-induced band tailing, the Elliott analysis provides a more intrinsic estimate of the bandgap by explicitly accounting for the exciton.

Further investigation of the optical properties was performed using temperature- and power-dependent steady-state PL at an irradiance of 100 mW cm^{-2}. Figure 2(a) shows the PL spectra obtained at 12 K for the three types of samples. The low temperature minimizes the thermal broadening of the PL line shape, thereby providing clearer insights into the defectivity of the samples. All spectra exhibit a main emission peak, likely due to excitonic recombination, that undergoes a progressive blueshift with increasing FABr excess, consistent with the trend observed in the absorption spectra. Notably, the Control sample shows an additional broad emission band at lower energy, indicative of significant defect-related sub-bandgap states.

Power-dependent PL was performed to identify the recombination mechanisms responsible for the low-energy emission at 12 K, distinguishing among defect-mediated, excitonic, and free-carrier recombination. The dependence of the PL intensity (I_{PL}) on the excitation power (I) follows a power-law behavior, which in logarithmic form can be expressed as:

$$\log_{10}(I_{PL}) = \log_{10}(A) + n\log_{10}(I) \tag{2}$$

where A is a proportionality constant and n is the power-law exponent that provides an indication of the recombination mechanism involved [34, 35]. Specifically, values of $n < 1$ indicate defect-mediated recombination, such as free-to-bound or donor-acceptor pair (DAP) recombination, n close to 1 indicates a purely excitonic recombination, while $n \approx 2$, suggests a dominant free carrier recombination. Intermediate values between 1 and 2 indicate the coexistence of excitonic and free-carrier recombination within the sample. Figure 2(b) reports the PL intensity of the main emission peak as a function of the excitation irradiance for all samples, together with the best-fit curves obtained using equation (2). The corresponding values of n are summarized in table 2.

The numbers reported in table 2 reveal changes of the dominant recombination mechanism upon FABr incorporation. The Control sample is primarily governed by defect-assisted recombination ($n < 1$), while the FABr +5% and FABr +10% films exhibit power-law exponents ($n \approx 1$) consistent with predominant excitonic emission. The reduction of defect-assisted recombination in FABr +5% and FABr +10% films is consistent with FABr-induced passivation of bromine vacancies and in agreement with what is observed in absorption. This confirms that both FABr-enriched films maintain a predominantly excitonic character of their optical properties, suggesting that the variations observed in their absorption spectra principally arise from broadening due to compositional disorder and thermal factors. FTAS

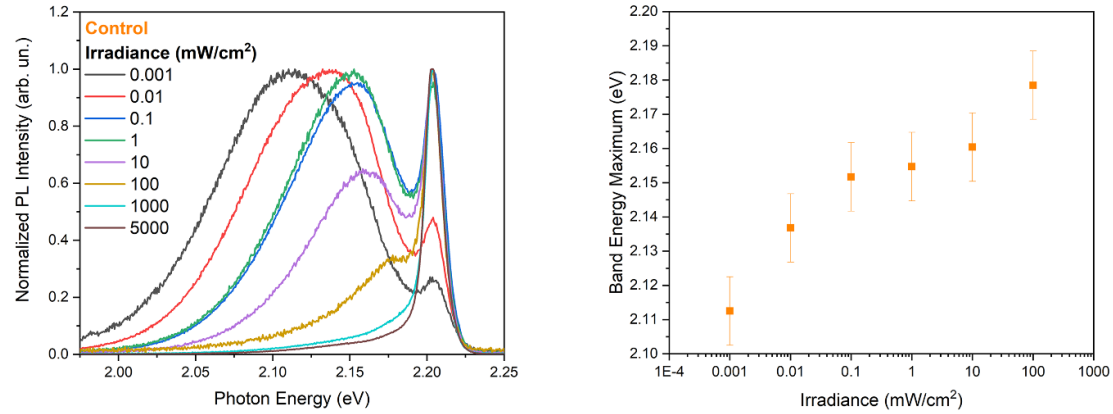


Figure 3. (a) PL spectra acquired at 12 K and normalized to their absolute maximum to facilitate comparison among different excitations; (b) band energy maximum of the low-energy PL peak of the control sample obtained as a function of selected irradiances of excitation.

and temperature-dependent PL measurements, reported in sections S.3 and S.4 of SI, corroborate this interpretation [36, 37].

To further clarify the role of defect states in the PL recombination of the Control sample, figure 3(a) displays the PL spectra recorded at 12 K and at selected excitations (0.001, 0.01, 0.1, 1, 10, 100, 1000, and 5000 mW cm^{-2}). Two distinct emission peaks are observed. The high-energy peak, centered at 2.20 eV, is attributed to excitonic recombination and exhibits no noticeable shift with excitation power. In contrast, the low-energy emission shows a clear blueshift as the excitation irradiance increases. Figure 3(b) reports the evolution of the low-energy peak position (center of mass) as a function of excitation irradiance. This behavior is characteristic of DAP recombination, involving electrons and holes bound to donors and acceptors. Hence, DAP recombination can be associated with the presence of complementary defect states, such as halide vacancies acting as donor-like centers and A-site vacancies acting as acceptor-like centers [38]. The energy of the emitted photons is expressed by the following equation:

$$E_{\mathrm{DAP}} = \left(E_{\mathrm{g}} - E_{\mathrm{D}^0} - E_{\mathrm{A}^0}\right) + \frac{e^2}{4\pi\,\epsilon;_0\epsilon_r} \cdot \frac{1}{r_{\mathrm{DA}}} \tag{3}$$

where E_{g} is the bandgap, E_{D0} and E_{A0} are the binding energies of electrons and holes to their respective donor and acceptor centers, and the last term accounts for the Coulomb interaction between the ionized centers after recombination [39–41].

While the first three terms are independent of excitation power, the Coulombic term is power dependent. As the laser intensity increases, a larger number of donors and acceptors become occupied, leading to a reduction of their average mutual distance r_{DA}. Consequently, the emission maximum of the DAP band exhibits a blueshift with increasing excitation power. This behavior is a fingerprint of DAP recombination and clearly different from excitation-induced thermal effects or other emission processes. The absence of a DAP band in the FABr +5% and FABr +10% samples indicates that FABr incorporation effectively reduces or passivates donors and acceptors.

These results indicate that the addition of FABr during film synthesis mitigates the defectivity of the films while promoting compositional disorder. Since these two effects compete in determining the overall film quality, SEM was used to evaluate how FABr excess influences the morphology of the perovskite layers.

Figures 4(a)–(c) show the top-view SEM images of Control, FABr +5% and FABr +10%, respectively. These images were analyzed using Gwyddion [29] to quantify the grain size distribution in the studied samples, as reported in figures 4(d)–(f). Given the almost hexagonal shape of the grains, their size was estimated by measuring the longest distance between two opposite edges. The analysis of the SEM images reveals that the introduction of FABr excess results in a marked reduction in grain size. While the Control and FABr +10% samples exhibit relatively narrow grain size distributions centered around ∼850 nm and ∼250 nm, respectively, the FABr +5% sample shows a much broader distribution, spanning from approximately 50 nm up to 1200 nm. This indicates that the morphology at 5% FABr excess is not drastically altered compared to the Control but rather consists of a heterogeneous

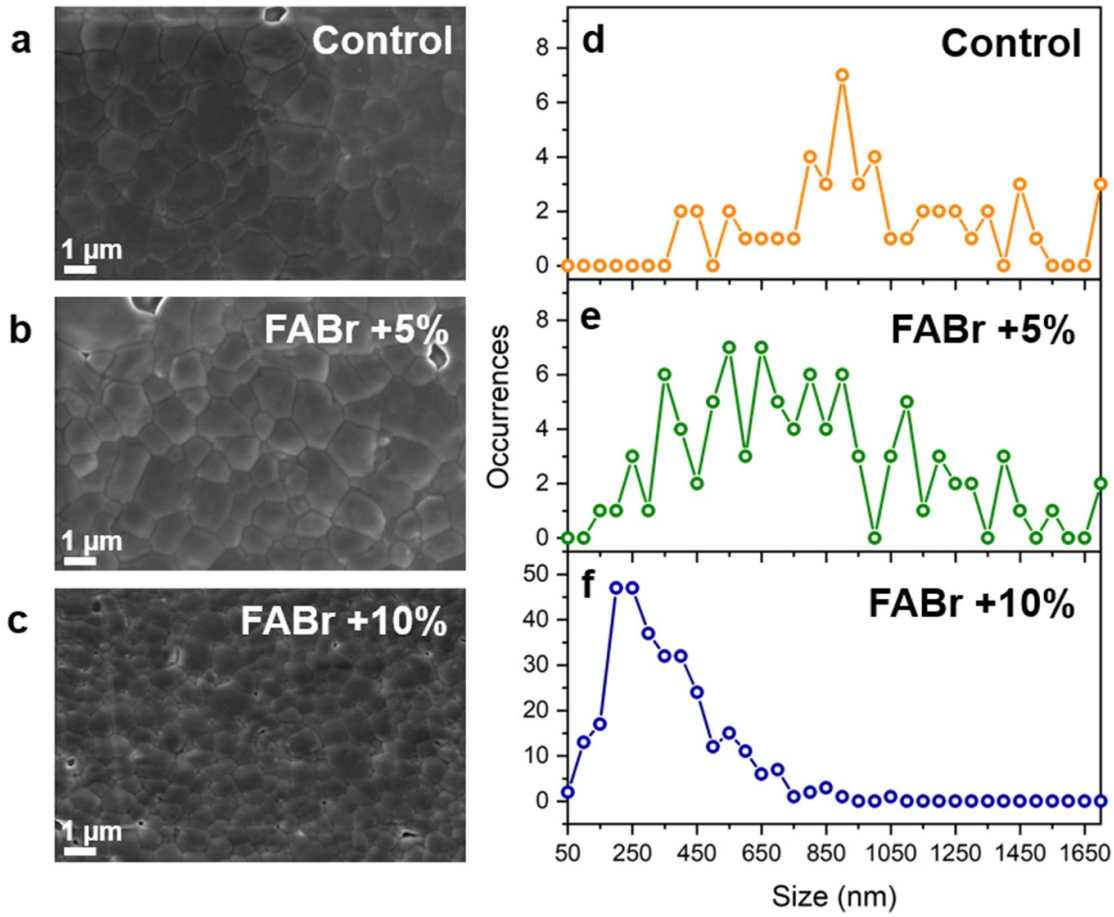


Figure 4. SEM images obtained for (a) control, (b) FABr +5% and (c) FABr +10%. Analysis of the grain sizes of (d) control, (e) FABr +5% and (f) FABr +10%.

microstructure where large grains are still present. Overall, the excess of FA reduces the grain size distribution compared to the Control sample. While the SEM images highlight pronounced changes in grain size and morphology upon FABr addition, XRD measurements were employed to probe whether these variations are reflected in the average crystal structure of the films. The XRD patterns of Control, FABr +5% and FABr +10%, reported in figure S3 of SI, exhibit the same set of crystalline reflections that demonstrate that all the samples show an α-$FAPbBr_3$ perovskite phase. No additional reflection or significant shift in the peak positions are observed with the excess of FABr, indicating that the bulk crystal structure and the average lattice parameter of $FAPbBr_3$ are preserved [28, 42]. Furthermore, the morphological changes revealed by the SEM analysis are in good agreement with the trends observed in the temperature-dependent PL (see section S.4 of SI). In particular, the broader FWHM of the PL emission in the FABr +10% sample correlates well with the reduced grain size and larger disorder visible in the SEM images. In addition, the PL peak energy of FABr +10% is consistently blue shifted relative to the Control at all temperatures, indicating that FABr excess alters the perovskite chemical composition in a way that significantly affects its optical properties.

Summarizing, the combined structural and spectroscopic results provide important insight into the origin of the observed optical trends. XRD analysis shows that all samples retain the same crystalline phase, with no evidence of secondary phases or measurable shifts in peak positions, indicating that both the crystal structure and the average lattice parameter remain essentially unchanged with increasing FABr content. This is consistent with the results of optical and ultrafast spectroscopies, which indicate that the fundamental electronic structure of the material is preserved. In particular, FTAS and temperature-dependent PL measurements confirm the dominant excitonic character across all compositions, while no additional recombination channels, typically associated with secondary phases, are observed. These observations suggest that lattice strain and secondary phases can be excluded as the primary origin of

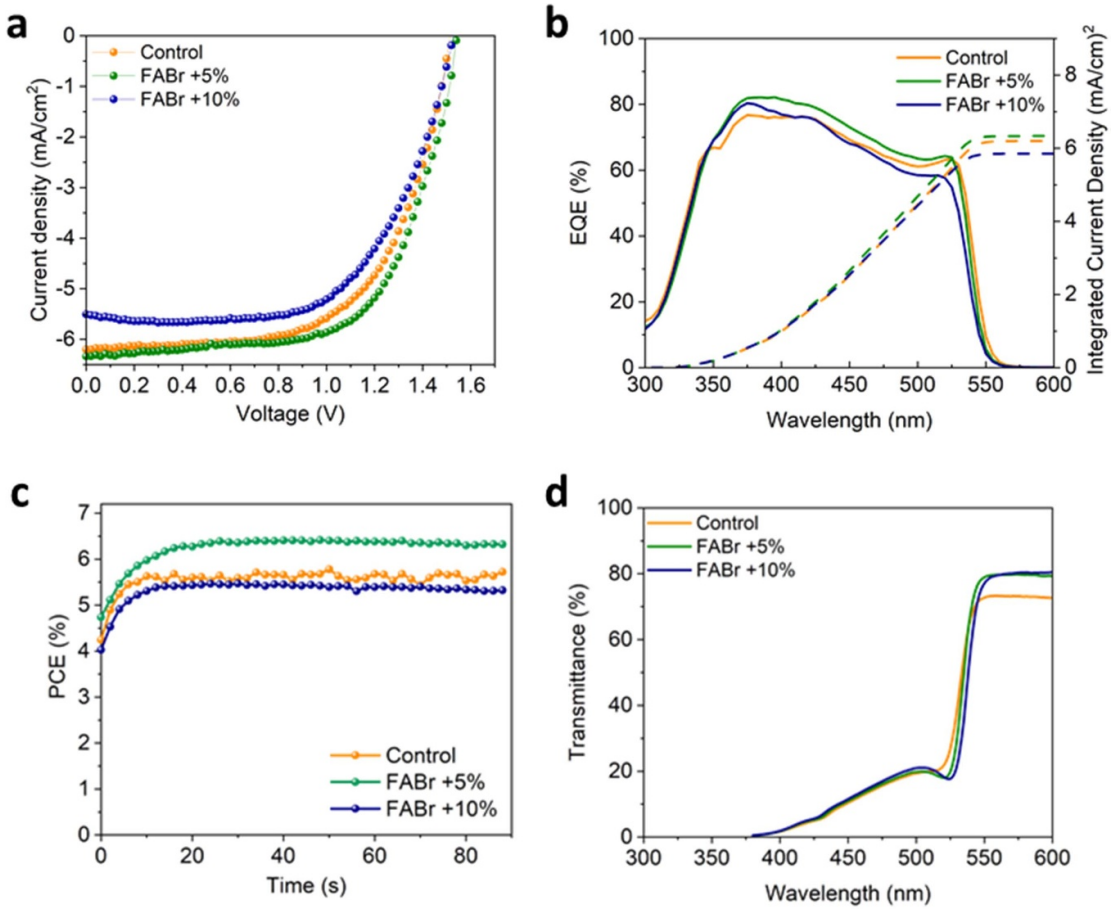


Figure 5. (a) *J*–*V* curves of the champion device measured in the reverse scan direction (see section S6 of the SI for further informations), (b) EQE (solid line) and integrated current density (dashed line) (c) 90-s maximum power point tracking (MPPT) and (d) transmittance obtained for control, FABr +5%, and FABr +10%.

the observed blueshift of the bandgap. Instead, the shift is more plausibly attributed to compositional variations induced by FABr excess.

To verify whether the spectroscopic findings are consistent with the performance of the photovoltaic devices, semitransparent solar cells based on the Control, FABr +5%, and FABr +10% films were fabricated. Figures 5(a)–(d) present the current–voltage (*J*–*V*) curves, the external quantum efficiency (EQE) spectra, 90-s maximum power point tracking (MPPT), and the transmittance for the three devices. See details in section S.6 of SI. The champion devices were also measured in both forward and reverse scan directions for all compositions, as reported in figure S4 in SI.

The measured short-circuit current density (J_{SC}), open-circuit voltage (V_{OC}), fill factor (FF), and power conversion efficiency (PCE) for all solar cells, together with their AVT and light utilization efficiency (LUE), are summarized in table 3. While PCE is the standard metric for evaluating photovoltaic performance, AVT and LUE are particularly important for semitransparent devices. AVT quantifies the average fraction of visible light transmitted through the device, whereas LUE, defined as the product of AVT and PCE, serves as a key figure of merit for semitransparent solar cells by capturing the trade-off between optical transparency and photovoltaic efficiency.

The Control and FABr +5% devices exhibit only limited hysteresis, whereas the FABr +10% sample shows a more pronounced scan-direction dependence. For the Control device, the PCE decreases from 5.77% in the reverse scan to 5.26% in the forward scan, mainly due to a reduction in FF (from 61.52% to 56.8%), while V_{OC} and J_{SC} remain nearly unchanged (from 1.51 to 1.50 V and from 6.20 to 6.15 mA cm^{-2}, respectively). The FABr +5% device delivers the best overall performance, with a PCE of 6.26% in the reverse scan and 5.60% in the forward scan, accompanied by a decrease in FF from 64.14% to 58.97%, while V_{OC} (1.54–1.53 V) and J_{SC} (6.33–6.18 mA cm^{-2}) remain almost constant. In contrast, the FABr +10% device exhibits the least favorable performance, with a reverse-scan PCE of 4.98% increasing to 5.29% in the forward scan, indicating significant scan-direction dependence. This behavior

Table 3. *J*sc, V_{OC}, FF, PCE, AVT, and LUE measured for the solar cells fabricated using active layers synthesized with the same stoichiometry of control, FABr +5%, and FABr +10%. *J*sc, V_{OC}, FF and PCE are measured in forward (FW) and reverse (RV) scan directions.

Material	Scan	J_{SC} (mA cm^{-2})	V_{OC} (V)	FF (%)	PCE (%)	AVT (%)	LUE (%)
Control	RV	6.20	1.51	61.52	5.77	60.2	3.47
	FW	6.15	1.50	56.8	5.26		
FABr +5%	RV	6.33	1.54	64.14	6.26	61.6	3.85
	FW	6.18	1.53	58.97	5.6		
FABr +10%	RV	5.85	1.52	53.76	4.98	58.4	3.09
	FW	5.50	1.53	62.94	5.29		

is associated with a large variation in FF (53.76% vs 62.94%) and a reduced photocurrent density compared to the other compositions. Figure 5(b) reports the EQE, confirming the measured current densities of the champion devices, while figure 5(c) shows stable MPPT over 90 s for all samples.

Statistical analysis supports these observations (figure S5 and table S1 in SI). In particular, the FABr +5% devices exhibit the highest average V_{OC} (1.56 V), with peak values exceeding 1.6 V, indicating a more effective suppression of non-radiative recombination. The control devices show a slightly lower average V_{OC} (1.54 V), consistent with less efficient defect passivation, while the FABr +10% samples do not show further improvement, instead exhibiting an average decrease of approximately 5%. This trend suggests that, beyond the optimal FABr excess, the beneficial reduction of defect-assisted recombination is progressively counterbalanced by increased structural and morphological disorder in the absorber. Notably, the same behavior is observed in both scan directions, confirming that the superior performance of the FABr +5% composition reflects a more robust and intrinsic device response rather than a measurement-dependent effect.

These results indicate that the FABr +5% sample achieves the optimal combination of PCE (6.26%), AVT (61.6%), and LUE (3.85%), reflecting a favorable balance between two competing effects induced by FABr excess: effective defect passivation, increase of compositional disorder, and grain size reduction. This finding underscores the critical influence of precursor stoichiometry on film formation and its decisive impact on the photovoltaic performance of the resulting devices.

4. Conclusions

In this study, we explored the impact of different levels of FABr over-stoichiometry introduced during the fabrication of wide-bandgap $FAPbBr_3$ perovskite films on the resulting morphology, optoelectronic properties, and device performance. We have demonstrated that even small compositional variations significantly influence both the structural and optical behavior of the resulting films.

Spectroscopic analyses revealed a consistent blueshift in the emission and absorption energy upon FABr addition, assigned to compositional variations induced by FABr excess, together with the reduction of defect-assisted recombination. In lead halide perovskites, bromine vacancies act as electron traps that locally distort the band structure, introducing sub-bandgap states and reducing the effective bandgap. The incorporation of FABr compensates for these vacancies, reducing the trap-state density and promoting a more uniform and defect-free lattice. As a result, non-radiative recombination is reduced—as shown by the absence of low-energy PL features and by the blueshift of the optical transition. The presence of DAP emission exclusively in the stoichiometric film further supports this interpretation. Its absence in FABr-enriched samples indicates effective defect passivation and the consequent suppression of sub-bandgap transitions.

Electron microscopy revealed a progressive reduction of grain size with increasing FABr content, associated with modified crystallization kinetics under excess precursor conditions. The FABr 5% composition provided the best compromise between low defect density and controlled morphological disorder, resulting in the most favorable film quality. This is reflected in device performance, with FABr 5% delivering the highest PCE (6.26%), AVT (61.6%), and LUE (3.85%).

In conclusion, we have shown that careful precursor engineering, specifically the introduction of controlled amounts of precursor over-stoichiometry, can substantially influence crystallization, defect density, and thus the optical and electronic quality of perovskite films of $FAPbBr_3$. Future work should focus on decoupling these competing effects, for instance, by combining stoichiometric tuning with

advanced crystallization control or interface engineering strategies. This approach could enable further improvements in both efficiency and operational stability, paving the way toward the integration of wide-bandgap perovskites in high-performance semitransparent and tandem photovoltaic devices.

Acknowledgment

S.T., G.A., D.C., P.O.K. acknowledge the European Union—NextGenerationEU, M4C2, within the PNRR project NFFA-DI, CUP B53C22004310006, IR0000015 for funding. The authors acknowledge the European Project 'Energy Harvesting in Cities with Transparent and Highly Efficient Window-Integrated Multi-Junction Solar Cells' (CITYSOLAR) for supporting the work, which received funding from the European Union's Horizon2020 research and innovation program under grant agreement number 101007084. J.B. acknowledges the support of the Project 'Network 4 Energy Sustainable Transition—NEST', Spoke 1, Project code PE0000021, funded under the National Recovery and Resilience Plan (NRRP), Mission 4, Component 2, Investment 1.3—Call for tender No. 1561 of 11.10.2022 of Ministero dell'Università e della Ricerca (MUR) funded by the European Union—NextGenerationEU. The authors acknowledge Dr Daniel Ory for sharing the fitting routine employed in the Elliot-based excitonic absorption model analysis of the absorption spectra.

Data availability statement

The data cannot be made publicly available upon publication because no suitable repository exists for hosting data in this field of study. The data that support the findings of this study are available upon reasonable request from the authors.

Supporting Information available at https://doi.org/10.1088/2632-959X/ae6f36/data1.

Author contributions

G Ammirati 0000-0002-4185-6222
Conceptualization (equal), Data curation (lead), Formal analysis (lead), Investigation (equal), Writing – review & editing (equal)

F Martelli 0000-0002-4496-4165
Investigation (equal), Methodology (equal), Supervision (equal), Writing – review & editing (equal)

F Toschi 0000-0002-7215-4805
Data curation (equal), Investigation (equal), Writing – review & editing (equal)

S Turchini 0000-0003-0122-0614
Funding acquisition (equal), Investigation (equal), Supervision (equal), Writing – review & editing (equal)

P O'Keeffe 0000-0002-8676-4436
Investigation (equal), Methodology (equal), Writing – review & editing (equal)

A Paladini 0000-0002-2059-1552
Investigation (equal), Methodology (equal), Writing – review & editing (equal)

F Matteocci 0000-0001-7893-1356
Conceptualization (equal), Data curation (equal), Investigation (equal), Methodology (equal), Writing – review & editing (equal)

J Barichello 0000-0003-1277-4217
Data curation (equal), Investigation (equal), Methodology (equal), Writing – review & editing (equal)

D Di Girolamo
Data curation (equal), Investigation (equal), Writing – review & editing (equal)

S Piccirillo 0000-0002-7938-6852
Investigation (equal), Writing – review & editing (equal)

A Di Carlo 0000-0001-6828-2380
Funding acquisition (lead), Supervision (equal), Writing – review & editing (equal)

D Catone 0000-0002-7649-2756
Conceptualization (equal), Funding acquisition (equal), Investigation (equal), Methodology (equal), Supervision (lead), Writing – original draft (lead), Writing – review & editing (lead)

References

[1] Zhang X, Turiansky M E, Shen J-X and Van de Walle C G 2022 Defect tolerance in halide perovskites: a first-principles perspective *J. Appl. Phys.* **131** 090901
[2] Miah M H, Khandaker M U, Rahman M B, Nur-E-Alam M and Islam M A 2024 Band gap tuning of perovskite solar cells for enhancing the efficiency and stability: issues and prospects *RSC Adv.* **14** 15876–906
[3] Jena A K, Kulkarni A and Miyasaka T 2019 Halide perovskite photovoltaics: background, status, and future prospects *Chem. Rev.* **119** 3036–103
[4] Adhyaksa G W P, Veldhuizen L W, Kuang Y, Brittman S, Schropp R E I and Garnett E C 2016 Carrier diffusion lengths in hybrid perovskites: processing, composition, aging, and surface passivation effects *Chem. Mater.* **28** 5259–63
[5] deQuilettes D W, Frohna K, Emin D, Kirchartz T, Bulovic V, Ginger D S and Stranks S D 2019 Charge-carrier recombination in halide perovskites: focus review *Chem. Rev.* **119** 11007–19
[6] Bi Y, Hutter E M, Fang Y, Dong Q, Huang J and Savenije T J 2016 Charge carrier lifetimes exceeding 15 Ms in methylammonium lead iodide single crystals *J. Phys. Chem. Lett.* **7** 923–8
[7] Anaya M, Galisteo-López J F, Calvo M E, Espinós J P and Míguez H 2018 Origin of light-induced photophysical effects in organic metal halide perovskites in the presence of oxygen *J. Phys. Chem. Lett.* **9** 3891–6
[8] Mathies F, Eggers H, Richards B S, Hernandez-Sosa G, Lemmer U and Paetzold U W 2018 Inkjet-printed triple cation perovskite solar cells *ACS Appl. Energy Mater.* **1** 1834–9
[9] Chen C *et al* 2022 Perovskite solar cells based on screen-printed thin films *Nature* **612** 266–71
[10] Howard I A, Abzieher T, Hossain I M, Eggers H, Schackmar F, Ternes S, Richards B S, Lemmer U and Paetzold U W 2019 Coated and printed perovskites for photovoltaic applications *Adv. Mater.* **31** 1806702
[11] Yang M *et al* 2017 Perovskite ink with wide processing window for scalable high-efficiency solar cells *Nat. Energy* **2** 1–9
[12] Matteocci F, Rossi D, Castriotta L A, Ory D, Mejaouri S, der Maur M A, Sauvage F, Cacovich S and Di Carlo A 2022 Wide bandgap halide perovskite absorbers for semi-transparent photovoltaics: from theoretical design to modules *Nano Energy* **101** 107560
[13] Subbiah A S, Mahuli N, Agarwal S, van Hest M F A M and Sarkar S K 2017 Towards all-inorganic transport layers for wide-band-gap formamidinium lead bromide-based planar photovoltaics *Energy Technol.* **5** 1800–6
[14] Zohar A, Kulbak M, Levine I, Hodes G, Kahn A and Cahen D 2019 What limits the open-circuit voltage of bromide perovskite-based solar cells? *ACS Energy Lett.* **4** 1–7
[15] Rajagopal A, Stoddard R J, Jo S B, Hillhouse H W and Jen A K-Y 2018 Overcoming the photovoltage plateau in large bandgap perovskite photovoltaics *Nano Lett.* **18** 3985–93
[16] Tao J, Zhao C, Wang Z, Chen Y, Zang L, Yang G, Bai Y and Chu J 2025 Suppressing non-radiative recombination for efficient and stable perovskite solar cells *Energy Environ. Sci.* **18** 509–44
[17] Campanari V *et al* 2022 Reevaluation of photoluminescence intensity as an indicator of efficiency in perovskite solar cells *Sol. RRL* **6** 2200049
[18] Elangovan N K, Kannadasan R, Beenarani B B, Alsharif M H, Kim M-K and Hasan Inamul Z 2024 Recent developments in perovskite materials, fabrication techniques, band gap engineering, and the stability of perovskite solar cells *Energy Rep.* **11** 1171–90
[19] Abdul Ghani I B, Khalid M, Hussain M I, Hussain M M, Ashraf R and Wang J 2022 Recent advancement in perovskite solar cell with imidazole additive *Mater. Sci. Semicond. Process.* **148** 106788
[20] Han E *et al* 2024 Efficient bifacial semi-transparent perovskite solar cells via a dimethylformamide-free solvent and bandgap engineering strategy *Nano Energy* **131** 110136
[21] Peng Y *et al* 2026 Synergistic defect passivation and phase stabilization enable highly efficient wide-bandgap perovskite solar cells and tandems *Nano Energy* **147** 111590
[22] Mei J and Yan F 2025 Recent advances in wide-bandgap perovskite solar cells *Adv. Mater.* **37** 2418622
[23] Zhang X, Huang H, Zhao C and Yuan J 2025 Surface chemistry-engineered perovskite quantum dot photovoltaics *Chem. Soc. Rev.* **54** 3017–60
[24] Bin Abdul Ghani I, Khalid M, Yan H, El Arfaoui Y, Nawaz B and Wang J 2025 Maximizing RbGeI3 perovskite solar cell efficiency through advanced TiO_2/Graphene nanocomposite electron transport layer *Optik* **320** 172116
[25] Abdul Ghani I B, Khalid M, Yan H, Kashif M, Nawaz B and Wang J 2024 Boosting $KSnI_3$-Based perovskite solar cell efficiency by 22.78% through optimized charge transport and eco-friendly buffer layer *J. Mater. Sci.* **59** 14547–72
[26] Son D-Y *et al* 2016 Self-formed grain boundary healing layer for highly efficient $CH_3NH_3PbI_3$ perovskite solar cells *Nat. Energy* **1** 16081
[27] Chen H *et al* 2020 High-efficiency formamidinium lead bromide perovskite nanocrystal-based light-emitting diodes fabricated via a surface defect self-passivation strategy *Adv. Opt. Mater.* **8** 1901390
[28] Di Girolamo D *et al* 2024 Breaking 1.7 V open circuit voltage in large area transparent perovskite solar cells using interfaces passivation *Adv. Energy Mater.* **14** 2400663
[29] Nečas D and Klapetek P 2012 Gwyddion: an open-source software for SPM data analysis *Open Phys.* **10** 181–8
[30] Catone D *et al* 2021 Effects of crystal morphology on the hot-carrier dynamics in mixed-cation hybrid lead halide perovskites *Energies* **14** 708
[31] O'Keeffe P, Ammirati G, Catone D, Pelli Cresi J S, Toschi F, Magnozzi M, Della Valle G, Bisio F and Paladini A 2024 Ultrafast dynamics of nonthermal carriers following plasmonic and interband photoexcitation of 2D arrays of gold nanoparticles *ACS Photonics* **11** 3205–12
[32] Ammirati G *et al* 2024 Unveiling the electronic band structure and temporal dynamics of excited carriers in formamidinium lead bromide perovskite *Adv. Opt. Mater.* **12** 2302013
[33] Ory D *et al* 2024 Effect of chlorine inclusion in wide band gap $FAPbBr_3$ perovskites *Adv. Opt. Mater.* **12** 2401212

[34] Schmidt T, Lischka K and Zulehner W 1992 Excitation-power dependence of the near-band-edge photoluminescence of semiconductors *Phys. Rev. B* **45** 8989–94
[35] Feng Z C, Mascarenhas A and Choyke W J 1986 Low temperature photoluminescence spectra of (001) CdTe films grown by molecular beam epitaxy at different substrate temperatures *J. Lumin.* **35** 329–41
[36] Milot R L, Eperon G E, Snaith H J, Johnston M B and Herz L M 2015 Temperature dependent charge carrier dynamics in $CH_3NH_3PbI_3$ perovskite thin films *Adv. Funct. Mater.* **25** 6218–27
[37] Woo H C, Choi J W, Shin J, Chin S-H, Ann M H and Lee C-L 2018 Temperature dependent photoluminescence of $CH_3NH_3PbBr_3$ perovskite quantum dots and bulk counterparts *J. Phys. Chem. Lett.* **9** 4066–74
[38] Meggiolaro D and De Angelis F 2018 First-principles modeling of defects in lead halide perovskites: best practices and open issues *ACS Energy Lett.* **3** 2206–22
[39] Hopfield J J, Thomas D G and Gershenzon M 1963 Pair spectra in GaP *Phys. Rev. Lett.* **10** 162–4
[40] Sivan A K, Di Mario L, Catone D, O'Keeffe P, Turchini S, Rubini S and Martelli F 2020 Plasmon-induced resonant effects on the optical properties of Ag-decorated ZnSe nanowires *Nanotechnology* **31** 174001
[41] Klingshirn C F 2012 *Semiconductor Optics* Graduate Texts in Physics (Springer)
[42] Tan W L and McNeill C R 2022 x-ray diffraction of photovoltaic perovskites: principles and applications *Appl. Phys. Rev.* **9** 021310